



Simulation of dislocation penetration through a general low-angle grain boundary

B. Liu, P. Eisenlohr, F. Roters, D. Raabe*

Max-Planck-Institut für Eisenforschung, Max-Planck-Straße 1, 40237 Düsseldorf, Germany

Received 23 March 2012; received in revised form 30 April 2012; accepted 1 May 2012

Available online 29 June 2012

Abstract

The interaction of dislocations with low-angle grain boundaries (LAGBs) is considered one important contribution to the mechanical strength of metals. Although LAGBs have been frequently observed in metals, little is known about how they interact with free dislocations that mainly carry the plastic deformation. Using discrete dislocation dynamics simulations, we are able to quantify the resistance of a LAGB—idealized as three sets of dislocations that form a hexagonal dislocation network—against lattice dislocation penetration, and examine the associated dislocation processes. Our results reveal that such a coherent internal boundary can massively obstruct and even terminate dislocation transmission and thus make a substantial contribution to material strength.

© 2012 Acta Materialia Inc. Published by Elsevier Ltd. All rights reserved.

Keywords: Dislocation dynamics; Strength; Low-angle grain boundary; Hexagonal dislocation network; Dislocation processes

1. Introduction

The development of the dislocation structure in crystal-line solids (having either face-centered cubic, body-centered cubic or hexagonal lattices) follows a universal evolution when starting from a state of low dislocation content up to large strains. The various structural components reach a dynamically equilibrated state after different amounts of strain. The most rapid development is the increase in content of free dislocations, which scales with flow stress. A concurrent but slower development is the growing density of low-angle grain boundaries (LAGBs) that accommodate the fragmentation of the crystallites [1–6]. Such fragmentation is inevitable because of spatially heterogeneous boundary conditions resulting from, for instance, variability in operable slip systems or grain neighborhood [7–9]. The average disorientation across LAGBs increases at an even lower rate and, after severe plastic deformation, ultimately transforms the subgranular structure into a high-angle grain boundary (HAGB)-dom-

inated polycrystal. At this stage, the spacing of HAGBs is closely related to the previously established LAGB spacing, which is found to scale (approximately) in inverse proportion to the saturation stress. The overall structural refinement entails a marked increase in deformation resistance, the majority of which is correlated to the increase in the LAGB density [1–6].

In order to capture the influence of LAGBs on strength and strain hardening in crystal plasticity, a fundamental understanding of their role is required. Comparable basic insights into materials strengthening have been provided by recent molecular dynamics (MD) and discrete dislocation dynamics (DDD) simulations of dislocation interactions (MD & DDD) [10–15], irradiation-induced hardening (MD & DDD) [16], thin metal and semiconductor films (DDD) [17,18], microscale size-dependent strengthening (DDD) [19–22], nanocrystalline metals (MD) [23–25] and nanoscale twin boundary strengthening (MD) [26,27].

The present work focuses on the ability of dislocations to penetrate general low-angle (coherent) grain boundaries. Penetration resistance has long been expected to be dominated by the local interaction between the incident

* Corresponding author. Tel.: +49 211 6792 340; fax: +49 211 6792 333.
E-mail address: d.raabe@mpie.de (D. Raabe).

and LAGB dislocations [28]. Given the strong dislocation interactions, particularly collinear annihilation [11] and ternary junctions [12] that can occur between incident and network dislocations, it is reasonable to believe that such a LAGB can make a substantial contribution to material strength.

The present paper studies the transmission of incident lattice dislocations through a LAGB using DDD simulations. The body-centered cubic (bcc) lattice structure is chosen primarily to avoid implementation difficulties associated with planar dislocation dissociation. A general LAGB is composed of two or more sets of mixed dislocations [28–30]. We idealize such a LAGB as a perfect regular mesh constructed from two sets of dislocations that relax into a hexagonal network by formation of $\langle 100 \rangle$ binary junctions. Assuming on average equal slip activity on all three possible slip system pairs that form binary junctions, networks containing the most stable mixed-symmetrical binary junction [31] would then be the most likely ones to occur.

The following aspects will be studied: (1) comparison of the transmission stresses for three incident dislocation types that undergo different reactions with the dislocation network; (2) dependence of transmission stress on the mobility of $\langle 100 \rangle$ dislocations; (3) dislocation processes occurring during network penetration.

2. Simulation details

2.1. Geometry

We use a modified version of the ParaDiS DDD code (developed at Lawrence Livermore National Laboratory [12,32]). The modification we have introduced consists of uncoupling the crystal and laboratory coordinate systems in order to be able to solve the dislocation–LAGB interaction problem in various laboratory frames [33]. The laboratory coordinate systems for the subsequent simulations are chosen such that (i) the X -axis coincides with the LAGB plane normal, (ii) the Z -axis runs along the intersection line between the incident slip plane and the LAGB plane, and (iii) the Y -axis follows as the cross-product of the first two axes (see Table 1). A cubic simulation box with edge length of $7200b$ (7200 times the magnitude of the Burgers

vector) is used, which is periodically extended in the X , Y and Z directions.

2.2. Low-angle grain boundary

Going beyond the idealized symmetrical tilt LAGB studied in Ref. [33], we construct the LAGB by relaxing two sets of parallel edge dislocations of type $1/2 [111](01\bar{1})$ and $1/2 [\bar{1}\bar{1}1](110)$, each set at an initial dislocation spacing of $200b$, on one plane in the center of the simulation box. The outer (“surface”) ends of each dislocation remain pinned during this relaxation and subsequent loading. The resulting equilibrated hexagonal network then contains three sets of mixed dislocations, namely the two starting ones and their reaction product $[010](101)$, which correspond to the red, blue and white segments, respectively, in Fig. 1. The dislocation content corresponds to a disorientation of about 0.3° across the LAGB. This small value is neglected in the kinematic set-up of the slip system geometries, i.e. the crystal orientation is identical on either side of the LAGB.

2.3. Selection of incident dislocations

The hexagonal dislocation network used here contains one set of $1/2 [111](01\bar{1})$ dislocations, one set of $1/2 [\bar{1}\bar{1}1](110)$ dislocations and the first-order binary junction $[010](101)$ as their reaction product. Possible reactions between an incident dislocation of type $1/2 \langle 111 \rangle \{110\}$ and all three hexagonal network dislocations are listed in Table 2 and comprise binary and ternary junction formations for red/blue and white network segments, respectively. Ternary dislocation interactions can be categorized into the two types: axial and zig-zag [34]. For the axial type interaction the two slip planes of the parents of the binary junction and the slip plane of the third $1/2 \langle 111 \rangle$ dislocation share a common intersection line. For the zig-zag type, this is not the case. Since the line direction of a binary junction typically remains close to that of the intersection line of its parent glide planes, the length of the axial ternary junctions is consequently longer than that of the zig-zag type.

In our case the four possible axial ternary reactions are:

1. $[010](101) + 1/2 [\bar{1}\bar{1}1](01\bar{1}) = 1/2 [\bar{1}\bar{1}\bar{1}](101)$
2. $[010](101) + 1/2 [\bar{1}\bar{1}1](101) = 1/2 [\bar{1}\bar{1}\bar{1}](101)$
3. $[010](101) + 1/2 [\bar{1}\bar{1}1](110) = 1/2 [\bar{1}\bar{1}\bar{1}](101)$
4. $[010](101) + 1/2 [\bar{1}\bar{1}1](101) = 1/2 [\bar{1}\bar{1}1](01\bar{1})$ or $1/2 [\bar{1}\bar{1}1](101)$ or $1/2 [\bar{1}\bar{1}1](110)$,

which correspond to items 1–4 in Table 2. The six reactions producing zig-zag ternary junctions are:

1. $[010](101) + 1/2 [111](01\bar{1}) = 1/2 [\bar{1}\bar{1}\bar{1}](101)$
2. $[010](101) + 1/2 [111](1\bar{1}0) = 1/2 [\bar{1}\bar{1}\bar{1}](101)$
3. $[010](101) + 1/2 [111](10\bar{1}) = 1/2 [\bar{1}\bar{1}\bar{1}](10\bar{1})$
4. $[010](101) + 1/2 [111](10\bar{1}) = 1/2 [111](10\bar{1})$

Table 1

Laboratory frames used in the simulations: X -axis parallel to LAGB plane normal $[13\bar{1}]$, Z -axis along the intersection line of the incident slip plane with the LAGB plane, and Y -axis perpendicular to the X and Z directions.

Incident dislocation	Color code	Laboratory frame		
		X	Y	Z
$1/2 [\bar{1}\bar{1}1](110)$	Black	$[13\bar{1}]$	$[7\bar{1}4]$	$[\bar{1}\bar{1}2]$
$1/2 [11\bar{1}](1\bar{1}0)$	Green	$[13\bar{1}]$	$[13\bar{5}2]$	$[114]$
$1/2 [111](1\bar{1}0)$	Red	$[13\bar{1}]$	$[13\bar{5}2]$	$[114]$

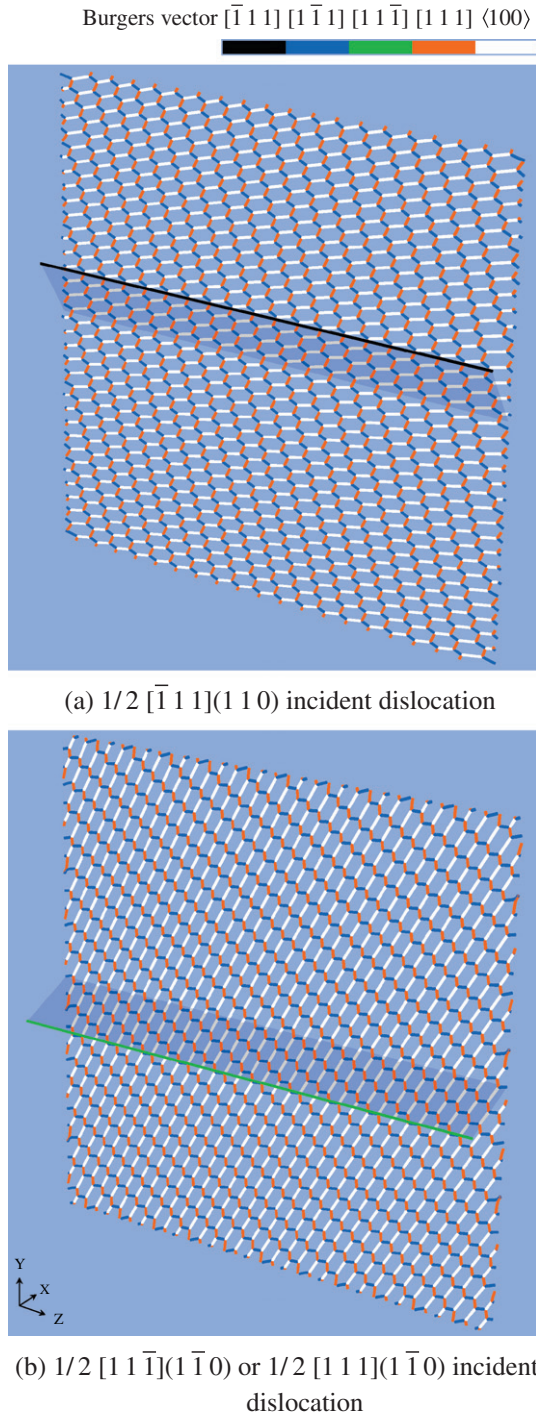


Fig. 1. Periodic initial configuration of the relaxed hexagonal dislocation network with different incident dislocations in the respective laboratory frames listed in Table 1. Semi-transparent planes illustrate the glide plane of the incident dislocation up to its trace with the dislocation network.

5. $[010](101) + 1/2 [111](1\bar{1}0) = 1/2 [1\bar{1}1](011)$
6. $[010](101) + 1/2 [1\bar{1}1](011) = 1/2 [111](1\bar{1}0)$,

and correspond to items 5–10 in Table 2.

The symmetry of the geometrical relations among the interacting dislocations reduces the twelve possible configu-

rations to only seven distinct cases as grouped in Table 2. From these, only four types of incident dislocations fulfill the requirement of having the same resolved shear stress for the network dislocations and for the incident one under both asymmetrical and symmetrical loading (load compatibility “+ + +” and “− + +” in Table 2). From these four, the self-interaction case is not explicitly considered, since it corresponds to a regular knitting-in or knitting-out process [35]. This leaves three types of incident dislocations termed “black”, “green”, and “red”, in accordance with their color in the DDD visualizations, corresponding to binary plus axial ternary, binary plus zig-zag ternary and binary (& col-linear) plus zig-zag ternary interactions, respectively.

A single incident dislocation (corresponding to a density of incident dislocations of $2 \times 10^{11} \text{ m}^{-2}$) is then placed at a slip distance of $10^3 b$ to the LAGB.

2.4. Loading conditions

Three uniaxial loading scenarios of initially 0.1 GPa normal stress along $[10\bar{1}]$, $[100]$ and $[01\bar{0}]$ are considered. Table 3 lists the Schmid factors experienced by the two network dislocation families and each of the three different incident dislocations under those three scenarios. For $[10\bar{1}]$ loading, the hexagonal network dislocations are free of external stress (zero Schmid factor). For $[100]$ loading, only the $1/2 [1\bar{1}1](110)$ set of network dislocations experiences a Schmid factor of 0.41 while the other set has a Schmid factor of zero. Finally, for $[01\bar{0}]$ loading, both sets of the $1/2 \langle 111 \rangle$ network dislocations are equally stressed and have a Schmid factor of 0.41. Every incident dislocation experiences a Schmid factor of 0.41 under all three loading conditions considered—except for the red incident dislocation remaining unstressed in the case of the unloaded network.

The applied stress is increased from its initial value of 0.1 GPa during the simulations at a rate of 10^5 GPa s^{-1} whenever the shear rate contributed by the incident dislocation density ρ falls below a reference rate $\dot{\gamma}_0$. This reference rate is taken as $\dot{\gamma}_0 = \rho_0 b v_0$ where ρ_0 is the initial value of the density and v_0 is the velocity of an isolated dislocation moving under a resolved shear stress of $0.41 \times 0.1 \text{ GPa}$.

2.5. Material parameters

ParaDiS uses isotropic elasticity. We adopt a shear modulus of $\mu = 82 \text{ GPa}$, a Poisson ratio of 0.29 and a Burgers vector of $b = 0.248 \text{ nm}$ to reflect bcc α -iron as an exemplary case. Typical discretization lengths for dislocation lines are in the range from 15 to $50b$. Cross-slip, pencil-glide and climb are excluded from this work. Dislocation mobilities $M_{\text{edge}} = M_{\text{screw}} = 1 \text{ Pa}^{-1} \text{ s}^{-1}$ are set isotropic for reasons of simplicity. Two cases are considered here in terms of the mobility ratio between dislocations of $\langle 100 \rangle$ and $1/2 \langle 111 \rangle$ Burgers vector: $M^{(100)}/M^{1/2 \langle 111 \rangle} = 1$ and 10^{-6} termed “mobile” and “immobile” $\langle 100 \rangle$ arms,

Table 2

Possible interactions among the dislocations constituting the hexagonal dislocation network (red, blue, white) and all incident dislocations of type $1/2 \langle 111 \rangle \{110\}$. “Load compatibility” indicates the fulfillment (“+”) of an initial Schmid factor of 0.41 for the incident dislocation under the three scenarios of none, asymmetrical, and symmetrical uniaxial loading, i.e. normal stress along $[10\bar{1}]$, $[100]$ and $[010]$, respectively. The “color code” alludes to the Burgers vector used for visualization of the DDD simulations. The naming scheme of binary junctions follows the work of Queyreau et al. [31].

Incident dislocation	Network dislocation			Load compatibility	Color code
	Red 1/2 [111](01 $\bar{1}$)	Blue 1/2 [1 $\bar{1}$ 1](110)	White [010](101)		
<i>Binary and axial ternary reactions possible</i>					
1/2 [$\bar{1}$ 11](01 $\bar{1}$)	Coplanar	Mixed-asymmetrical	Axial	+ + −	Black
1/2 [$\bar{1}$ 11](110)	Mixed-asymmetrical	Coplanar	Axial	+ + +	
1/2 [$\bar{1}$ 11](101)	Mixed-asymmetrical	Mixed-asymmetrical	Axial	+ − +	
1/2 [11 $\bar{1}$](101)	Mixed-symmetrical	Mixed-symmetrical	Axial	− − +	
<i>Binary and zig-zag ternary reactions possible</i>					
1/2 [11 $\bar{1}$](011)	Edge	Mixed-asymmetrical	Zig-zag	+ + −	Green
1/2 [11 $\bar{1}$](1 $\bar{1}$ 0)	Mixed-asymmetrical	Edge	Zig-zag	+ + +	
1/2 [111](10 $\bar{1}$)	Collinear annihilation	Mixed-asymmetrical	Zig-zag	− − +	
1/2 [1 $\bar{1}$ 1](10 $\bar{1}$)	Mixed-asymmetrical	Collinear annihilation	Zig-zag	− − +	
1/2 [111](1 $\bar{1}$ 0)	Collinear annihilation	Edge	Zig-zag	− + +	Red
1/2 [1 $\bar{1}$ 1](011)	Edge	Collinear annihilation	Zig-zag	− + −	
<i>Self interaction</i>					
1/2 [111](01 $\bar{1}$)	Self	Mixed-symmetrical	−	− + −	
1/2 [1 $\bar{1}$ 1](110)	Mixed-symmetrical	Self	−	− + +	

Table 3

Schmid factors of the red $1/2 [111](01\bar{1})$ and blue $1/2 [1\bar{1}1](110)$ network dislocation families and any of the incident dislocations under the three unidirectional loading scenarios investigated here.

Loading		Schmid factor		
Name	Direction	Network red	Network blue	Incident
None	$[10\bar{1}]$	0	0	0 (red) 0.41
Asym.	$[100]$	0	0.41	0.41
Sym.	$[010]$	0.41	0.41	0.41

respectively [33]. Note that $\langle 100 \rangle$ dislocations, which form as a reaction product between the two initial network dislocation sets, are usually treated as immobile dislocations for simplicity in DDD simulations (e.g. [12]) irrespective of the fact that MD simulations identified $\langle 100 \rangle$ dislocations as mobile [36,37]. Immobile $\langle 100 \rangle$ arms are considered here as a theoretical reference configuration.

3. Results

3.1. Determination of transmission stress

The dislocation penetration simulations start at a level of external stress that is well below the values expected at penetration [33]. At that (constant) initial stress the shear rate contributed by the incident dislocation eventually decreases once the motion of the incident dislocation gets impeded by the LAGB. The proper way to establish the transmission stress would be to incrementally raise the applied stress whenever this shear rate drops to zero, i.e. establishing a quasi-static situation. However, this approach is computationally very expensive due to the long

deceleration times to be followed in such simulations. Therefore, a different approach is taken by which the initially relatively low external stress is increased at a rate of 10^5 GPa s^{-1} as long as the shear rate remains below the threshold value $\dot{\gamma}_0$.¹ As a reaction to the gradually increasing stress, a spatially complex pattern of growing dislocation activity is observed upon penetration of the incident dislocation through the LAGB disturbed by it. Pinpointing the exact moment when a penetration event is actually triggered is not possible without some inherent ambiguity. However, roughly similar values resulted from either (subjectively) attempting to identify the onset of penetration by visual inspection of the evolution of dislocation activity during the stress increase, or by taking the final stress value at which the shear rate consistently remains above the threshold value. We estimate the accuracy of the penetration stress levels determined by the latter (objective) criterion to be about 50 MPa, which is sufficient to allow for a quantitative discrimination among the various penetration scenarios investigated in this paper.

3.2. General interaction outcomes

Three different interaction scenarios have been observed in the present investigation. For 20 out of the simulated 32 combinations, the incident dislocation is found to ultimately penetrate the hexagonal dislocation network. The respective penetration stresses are given in Table 4. In the six cases of an incident dislocation with positive sign, and only one out of the two network dislocation families being

¹ Considering the time step size as 10^{-10} – 10^{-9} s in these simulations, the stress increase per time step is small and in the range of 10–100 kPa.

Table 4

Resistance of the hexagonal network against penetration by different incident dislocation types for the three investigated loading scenarios and two different $\langle 100 \rangle$ mobilities. The uncertainty is estimated to be of the order of 50 MPa. Cases of network disintegration prior to a penetration of the incident dislocation are indicated by “ \ddagger ”. Co-motion of the (positive) incident dislocation with the network instead of penetration through it is indicated by “ \rightsquigarrow ”.

Loading		$\langle 100 \rangle$ arm mobility	Penetration resistance (GPa)					
Name	Direction		Black $1/2 [\bar{1}11](110)$		Green $1/2 [11\bar{1}](1\bar{1}0)$		Red $1/2 [111](1\bar{1}0)$	
			+	–	+	–	+	–
None	$[10\bar{1}]$	Immobile	0.38	0.56	0.45	0.41	–	–
		Mobile	0.37	1.1	0.63	0.56	–	–
Asym.	$[100]$	Immobile	\rightsquigarrow	0.52	\rightsquigarrow	0.36	\rightsquigarrow	\ddagger
		Mobile	\rightsquigarrow	\ddagger	\rightsquigarrow	0.53	\rightsquigarrow	\ddagger
Sym.	$[010]$	Immobile	0.38	0.66	0.46	0.42	0.59	\ddagger
		Mobile	0.37	\ddagger	0.64	0.57	0.82	\ddagger

loaded (termed “asymmetrical”), the network moves in the same direction as the incident dislocation. Under such conditions, the network partly separates from the locked set of nodes at its perimeter and subsequently disintegrates prior to the incident dislocation touching the network. This situation is indicated by “ \rightsquigarrow ” in Table 4. In another six cases, designated by “ \ddagger ” in Table 4, the applied stress reaches such a high level that the two network dislocation families unzip their (white) binary junctions, i.e. the network disintegrates, before the incident dislocation is able to penetrate.

3.3. Network stability against incident dislocation penetration

Table 4 reveals three major categories of resistance: (i) low resistance characterized by values around 0.4 GPa; (ii) intermediate resistances reaching values up to 0.8 GPa; and (iii) high resistances whose values come close to or even exceed the intrinsic stability limit of the hexagonal dislocation network. The latter case (stability of the network is exceeded) occurred for the situation of negative $1/2 [\bar{1}11](110)$ (black) and negative $1/2 [11\bar{1}](1\bar{1}0)$ (red) incident dislocations where the disintegration of the network happens prior to a successful penetration event (as indicated by “ \ddagger ” in Table 4).

The transmission stress is clearly dependent on the loading condition, mostly affected by the mobility of the $\langle 100 \rangle$ dislocations, and dominated by the type of the incident dislocation (interaction type and line sense).

3.4. Dislocation reactions between incident dislocations and hexagonal network

In this section we investigate the different penetration resistance values observed for the various configurations. More specifically, we analyze more closely the dislocation reactions occurring between the incident and network dislocations.

The collinear interaction was found to be the strongest among all binary dislocation interactions [11]. It can occur for incident dislocations sharing the Burgers vector of one of the $1/2\langle 111 \rangle$ network dislocations, but gliding on a

different slip plane. If the Burgers vector of the incident dislocation is different from both $1/2 \langle 111 \rangle$ network Burgers vectors, a ternary junction can be formed. Ternary dislocation junctions were discovered and studied by Bulatov et al. [12], and their average strengths are generally higher than those of binary junctions [34].

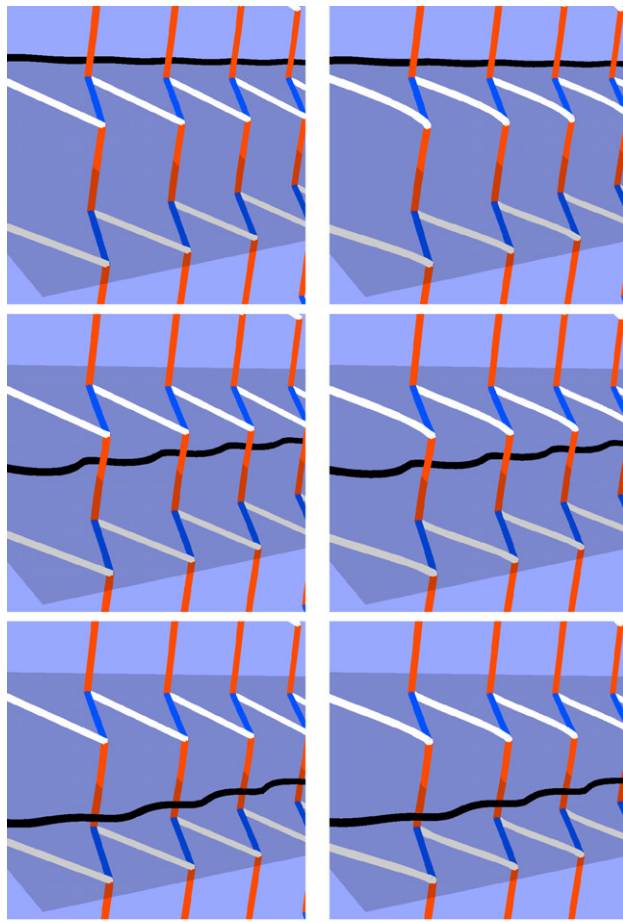
3.4.1. Black incident $1/2 [\bar{1}11](110)$ dislocation

The penetration resistances for the negative and positive incident black dislocations are largely different (see Table 4). The positively signed dislocation is penetrating at around 0.4 GPa and virtually unaffected by the $\langle 100 \rangle$ junction mobility. The negatively signed dislocation can penetrate at around 0.6 GPa when the binary $[010](101)$ network dislocations are set to be immobile. For mobile binary network dislocations the network disintegrates prior to any successful penetration except for the case of the unloaded network for which penetration at about 1.1 GPa is observed.

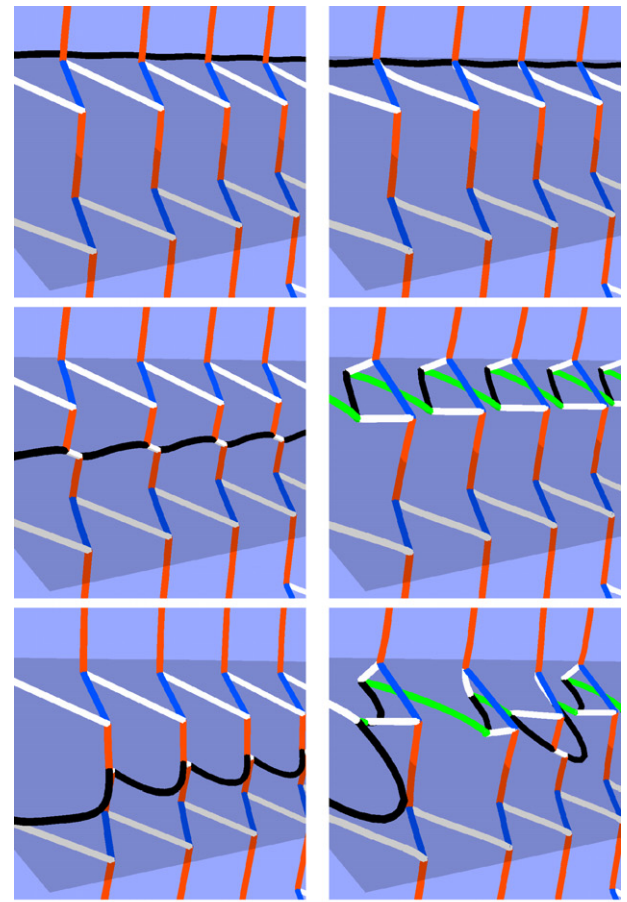
Figs. 2 and 3 contrast essential frames of the penetration sequence for the positive and negative black dislocations taking the unloaded network as an exemplary case. Subfigures (a) and (b) depict the situation for immobile and mobile $\langle 100 \rangle$ junctions, respectively. We chose to have the incident dislocation intersect the network in the center of the red segments since due to the kinked geometry of the dislocation network, incident black dislocations most frequently cut through red network segments but not through regions where both blue and white segments are present.

Fig. 2 reveals that the positive incident black dislocation is repelled by the red network dislocations and does not form any reaction product with them, irrespective of whether the segments are immobile or mobile $\langle 100 \rangle$. In both mobility cases, ultimate penetration is therefore achieved at comparably low stresses of about 0.4 GPa as is also observed for the case of symmetrically stressed network dislocations (see Table 4).

The situation for the negative incident dislocation, shown in Fig. 3, is quite different since this dislocation can form (long) axial ternary reactions with the white (binary) network segments. If the mobility of white segments is restricted, the incident dislocation cuts the network at red segments and



(a) **immobile** $\langle 100 \rangle$ junctions (b) **mobile** $\langle 100 \rangle$ junctions



(a) **immobile** $\langle 100 \rangle$ junctions (b) **mobile** $\langle 100 \rangle$ junctions

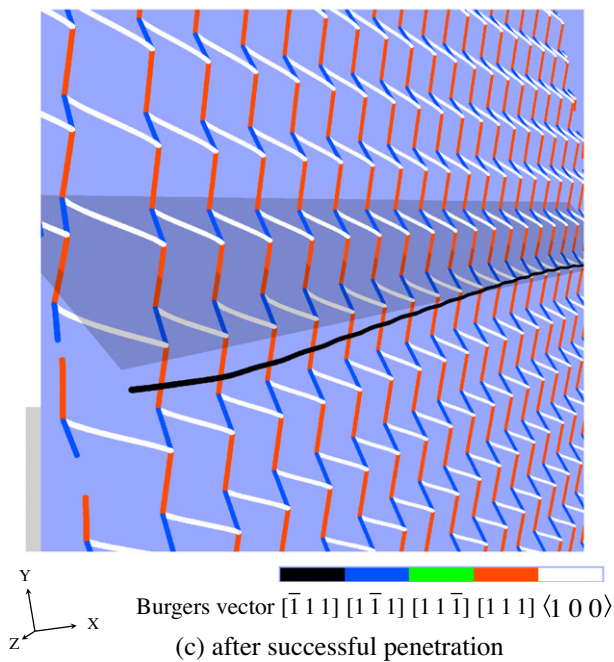


Fig. 2. Network penetration sequence of **positive** $1/2 [\bar{1}11](110)$ incident dislocation (on semitransparent glide plane). Vertical gray bar indicates stress (full height = 1.5 GPa).

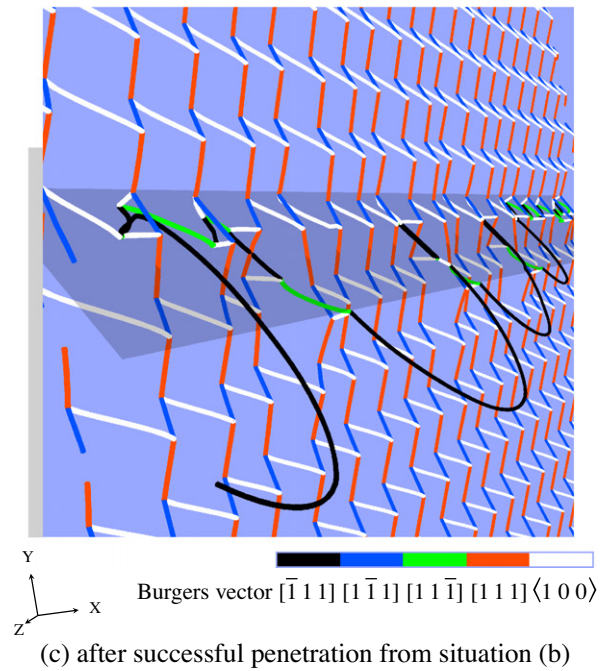


Fig. 3. Network penetration sequence of **negative** $1/2 [\bar{1}11](110)$ incident dislocation (on semitransparent glide plane). Vertical gray bar indicates stress (full height = 1.5 GPa).

produces short $[100](01\bar{1})$ mixed-asymmetrical binary junctions (white in Fig. 3a). Such junctions can be rather easily unzipped at a penetration stress of about 0.6 GPa. However, for the more realistic case of mobile binary junctions the existing white junctions bow out from the network, intercept the incident black dislocation, and react into $1/2 [11\bar{1}](101)$ ternary junctions (green in Fig. 3b).² Unzipping of these more stable ternary junctions could only be observed for the unloaded network case at stresses in excess of 1.1 GPa (see Fig. 3c). If the dislocation network was stressed, i.e. in the asymmetrical and symmetrical loading case, then disintegration of the network occurred prior to a penetration of the negative incident dislocation.

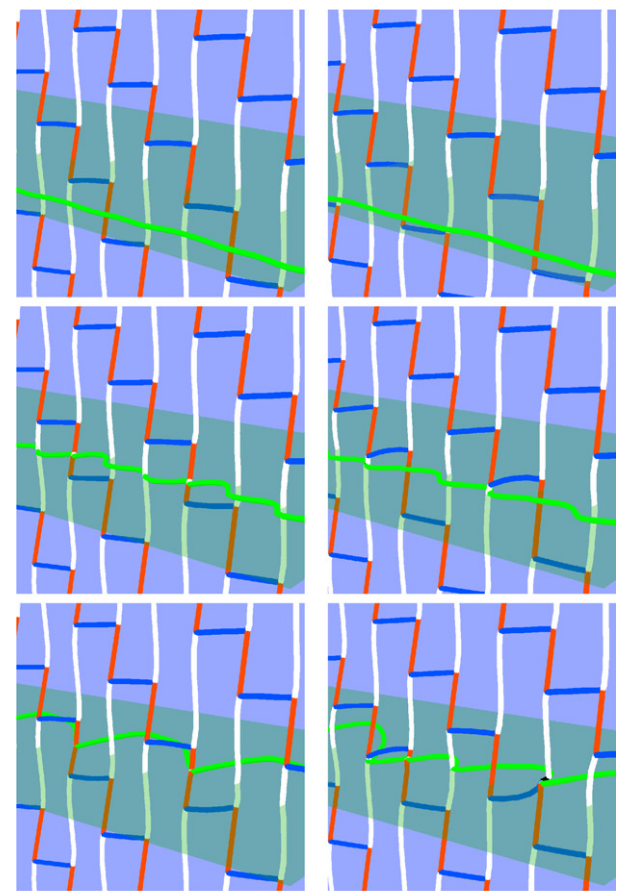
For both incident dislocation signs, the LAGB network was left intact upon successful penetration as, for instance, demonstrated in Figs. 2c and 3c.

3.4.2. Green incident $1/2 [11\bar{1}](1\bar{1}0)$ dislocation

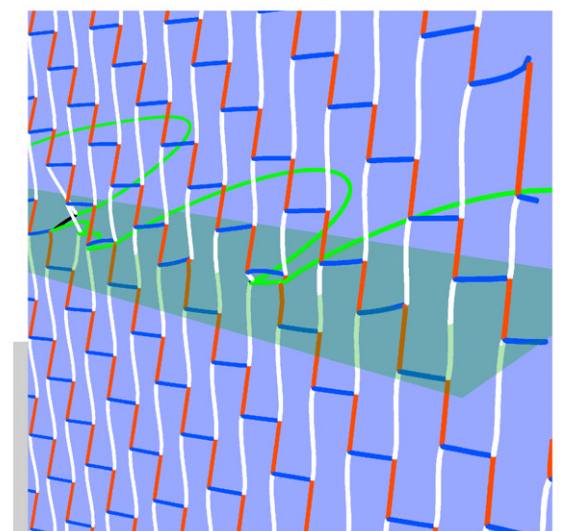
The penetration resistance values for both the positive and the negative green incident dislocations are very similar and do not depend substantially on the mobility of binary junctions or on the network load (see Table 4). Taking the unloaded network as an example, Figs. 4 and 5, we depict the penetration sequence for both signs of incident dislocations, with subfigures (a) and (b) contrasting the cases of low vs. high $\langle 100 \rangle$ mobility.

Both signs of the incident dislocation can form junctions with the dislocation network: the weakest ones, causing about 0.4 GPa in penetration resistance, are the short binary $[001](1\bar{1}0)$ mixed-asymmetrical junctions (white in Fig. 4a) that are formed between the negative incident and red network dislocations. Longer binary $[100](010)$ edge junctions (white in Fig. 5a) are formed between the positive incident and the blue network dislocations. The latter ones slightly increase the penetration resistance to 0.45 GPa. Cutting of the immobile pre-existing binary network segments does not create any substantial additional resistance in either case. If the pre-existing binary junctions are considered mobile, then additional reactions of these with the incident dislocation in $1/2 [\bar{1}11](101)$ ternary junctions (zig-zag type, black in Figs. 4b and 5b) are possible. These are shorter than the axial-type junctions observed for black incident dislocations, and therefore only cause a small increase in penetration resistance to about 0.6 GPa. Since the formation of ternary junctions leads to a net reduction of $\langle 100 \rangle$ binary junctions it can occur even when the intersecting dislocations are repulsive (Fig. 4b).

For both incident dislocation signs, a successful penetration event leaves the network in a virtually unaltered state with such examples shown in Figs. 4c and 5c.



(a) immobile $\langle 100 \rangle$ junctions (b) mobile $\langle 100 \rangle$ junctions



(c) after successful penetration from situation (b)

Fig. 4. Network penetration sequence of **negative** $1/2 [11\bar{1}](1\bar{1}0)$ incident dislocation (on semitransparent glide plane). Vertical gray bar indicates stress (full height = 1.5 GPa).

3.4.3. Red incident $1/2 [111](1\bar{1}0)$ dislocation

The penetration resistance for the red incident dislocation is highest among the three types simulated here

² This finding of easy formation of axial ternary junctions between (attractive) binary junctions and $1/2 [111]$ dislocation was also observed by Bulatov et al. [12]. However, in their case the binary junction was immobile but the $1/2 [111]$ dislocation was allowed to pencil-glide.

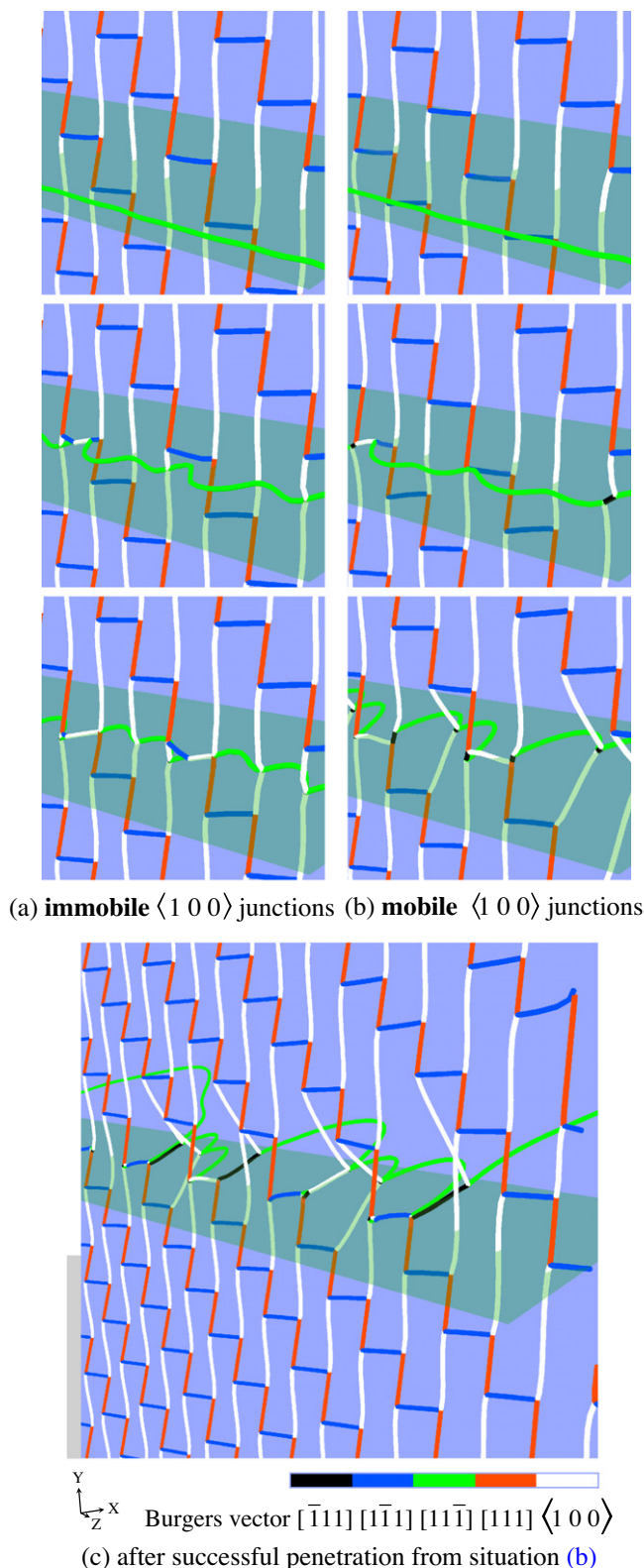


Fig. 5. Network penetration sequence of **positive** $1/2 [111](110)$ incident dislocation (on semitransparent glide plane). Vertical gray bar indicates stress (full height = 1.5 GPa).

(Table 4). This is not unexpected, since in addition to the formation of edge binary junctions and zig-zag ternary

junctions, the very strong reaction of collinear annihilation [11] can occur (Table 2).

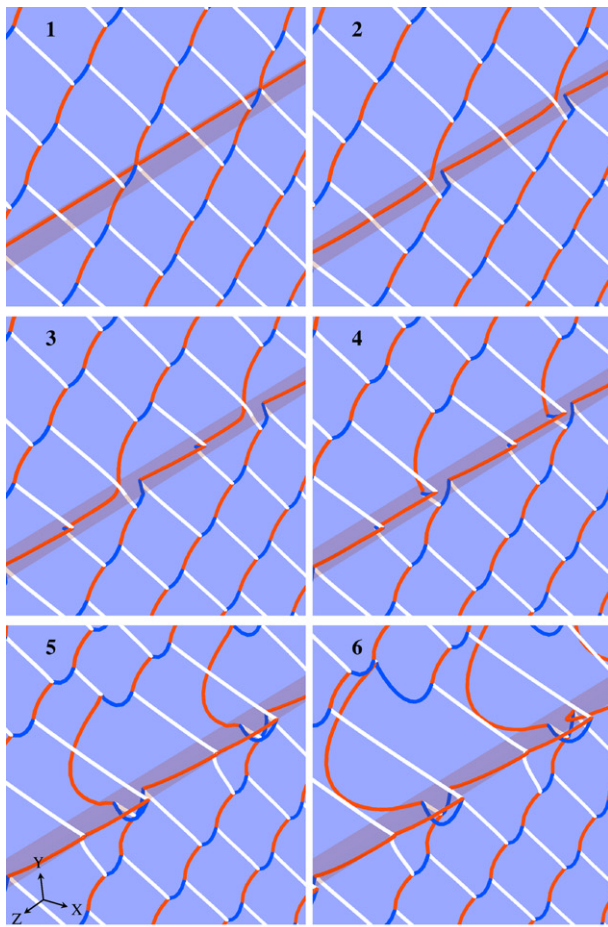
The red incident dislocation is not activated under $[10\bar{1}]$ loading, and the simulation results are elucidated here for the symmetric loading case where red and blue network dislocations experience the same resolved shear stress as the incident one.

For the positive incident dislocation, Fig. 6a presents six consecutive snapshots showing the evolution of the network up to the final penetration depicted in Fig. 6b. Between images 1 and 2 in Fig. 6a the incident dislocation first twisted, then annihilated short pieces of the red network, and thus shifted the connectivity of red segments by 2 at each location of incidence. A subsequent reaction of the incident dislocation with the (white) binary network segments shown in images 3 and 4 results—according to $1/2 [111](110) + [010](101) = 1/2 [1\bar{1}1](011)$ —in the formation of a set of blue segments (zig-zag ternary junction) that have a different slip plane to the blue network segments. With further increasing the stress to 0.82 GPa, the incident dislocation is ultimately able to penetrate the network (see Fig. 6b). After penetration, the intermediately formed blue segments recover at those locations where the incident dislocation has left the network. The penetration of the positive incident dislocation induces a coarser mesh region, where the activated red $1/2 [111](01\bar{1})$ and blue $1/2 [1\bar{1}1](110)$ network dislocations bow out and tear up the network (see Fig. 6b). The simulation results in the case of immobile $[010](101)$ network dislocations are not shown here. The immobile $[010](101)$ network dislocations cannot reorient and form zig-zag ternary junctions with the positive incident dislocation. The penetration occurs at a lower stress level of 0.59 GPa and does not induce network destruction.

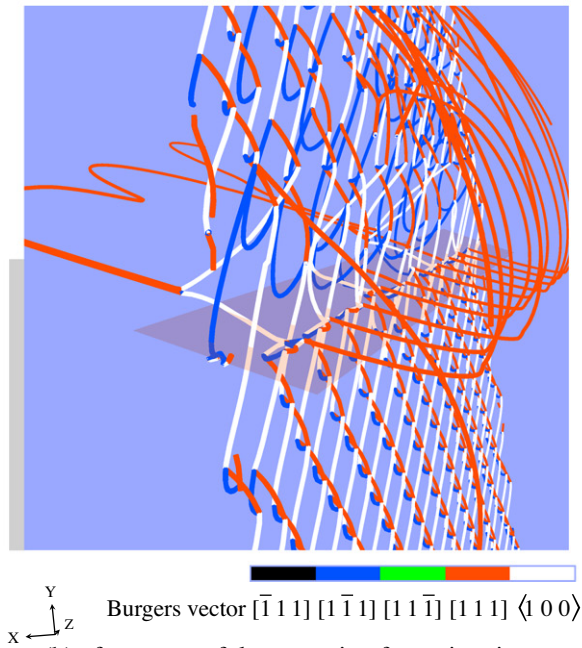
Fig. 7a gives an analogous sequence as Fig. 6a but for the negative incident dislocation. Because the line direction is opposite in this case, annihilation of red network segments occurs directly (see images 1 and 2), i.e. without the need of twisting. During further propagation of the incident dislocation (images 2–4) binary edge junctions are formed—following $1/2 [111](110) + 1/2 [1\bar{1}1](110) = [010](100)$ —with the available blue network dislocations. This results in reconnection of red and white network segments. At the end of this process (image 6) only the short red segments on the semitransparent glide plane remain of the incident dislocation. Because of this almost complete annihilation, an increase in stress does not reactivate the incident dislocation but unzips the two families making up the network, thus disintegrating the LAGB as shown in Fig. 7b. The simulation results of the negative incident dislocation are not affected by the mobility of $[010](101)$ network dislocations.

4. Discussion

The observed penetration resistances reflect the relative strength of the reaction products formed between the inci-

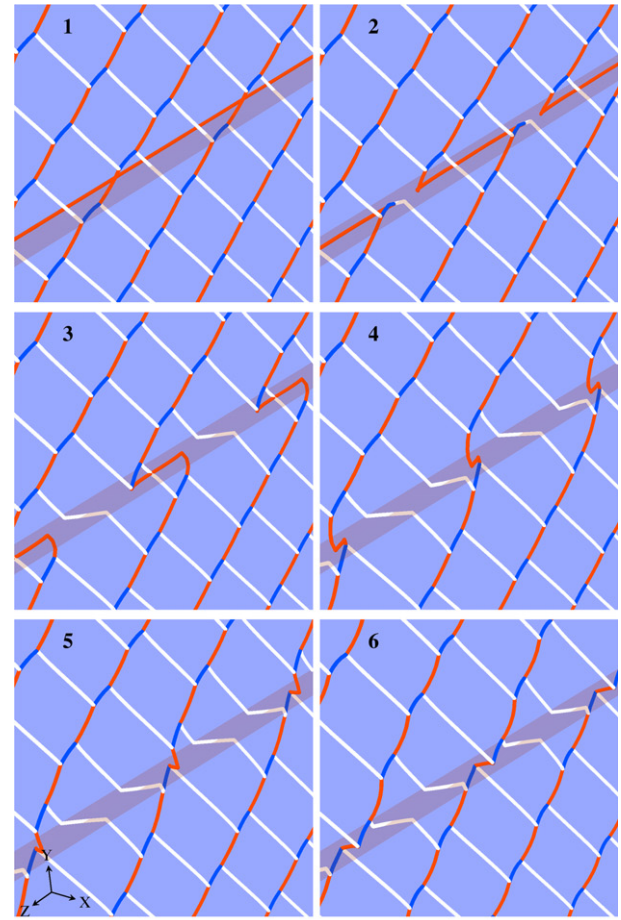


(a) twist annihilation of incident dislocation

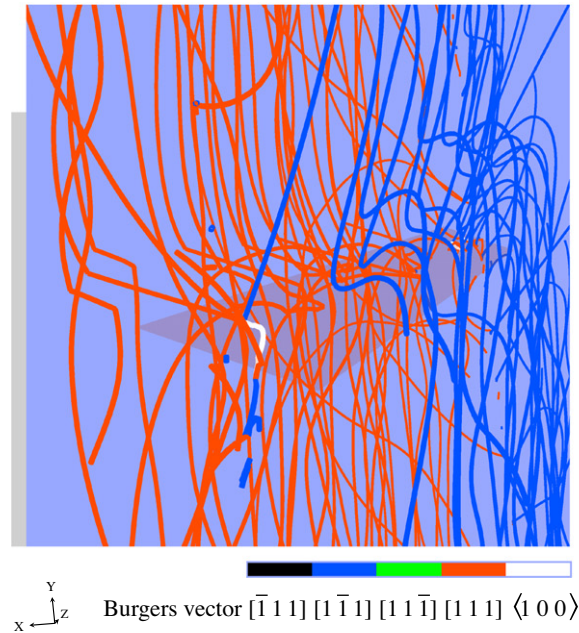


(b) after successful penetration from situation (a)

Fig. 6. Network penetration sequence of **positive** $1/2 [111](1\bar{1}0)$ incident dislocation (on semitransparent glide plane). Vertical gray bar indicates stress (full height = 1.5 GPa).



(a) direct annihilation of incident dislocation



(b) final network disintegration precedes penetration.

Fig. 7. Network penetration sequence of **negative** $1/2 [111](1\bar{1}0)$ incident dislocation (on semitransparent glide plane). Vertical gray bar indicates stress (full height = 1.5 GPa).

dent and network dislocations. Strong interactions, such as collinear annihilation or ternary junction formation, might even prevent dislocation penetration altogether. Generally speaking, the calculated penetration resistances are large compared to experimental flow stress values of pure α -iron [38–43]. This is particularly evident when it is considered that the selected disorientation across the simulated LAGB is of the order of only 0.3° . Penetration stresses σ are expected [44] to further increase with increasing disorientation (i.e. decreasing dislocation spacing s in the LAGB) according to the scaling relation $\sigma \propto (s/b)^{-1} \ln(s/b)$. The stress required locally in order for incident dislocations to penetrate (idealized) LAGBs up to a few degrees of disorientation thus ranges from small fractions of a GPa to some GPa as illustrated in Fig. 8. It is likely that this magnitude is independent of temperature, since the contribution of thermal activation to breaking the governing junctions is expected to be very small [42]. Therefore, as viewed from the perspective of a LAGB, the population of incident dislocations ranges from penetrating to getting stuck. From the opposite perspective, an incident dislocation experiences the LAGB population as ranging from transparent to not transparent. Comparing the transmission resistances in Table 4, this disparity can even occur for the same dislocation type but opposite line sense when approaching a given boundary.

Based on these findings and consistent with a number of experimental observations, low-angle grain boundaries have to be considered as major obstacles to homogeneous dislocation slip. The (temporary) holding up of dislocations traveling from one subgrain to a neighboring subgrain causes a plastic incompatibility between them that naturally gives rise to a heterogeneous field of internal stress [45,46].

This stress field would be expected to be highest close to the boundary and decaying towards the subgrain interior. Bulk measurements based on X-ray diffraction and convergent beam electron diffraction support this view (e.g. [47–49]). The direct observation of frozen-in radii of bowed-out dislocations in Al–5 wt.% Zn right at LAGBs indicates

that local stress values indeed exceed the applied stress by about an order of magnitude [50,51]. The strengthening contribution of LAGBs is also responsible for the primary transient during creep. During this transient, the dislocation density in the subgrain interior remains essentially constant [52]. On the other hand, a continuing build up of the subgrain structure and a gradually increasing LAGB disorientation is still observed (e.g. [53–55]) and result in the increase of deformation resistance. Recently, Mekala et al. [56] compared the transients of creep rate in response to sudden stress drops carried out in the primary transient and in steady state.³ They observed the transient strain required to recover the deformation resistance to increase along the primary transient, thus confirming the link between deformation resistance and (i) area per volume of LAGBs plus (ii) their internal densification.

LAGBs, on the other hand, cannot be completely non-transparent to slip transmission. The direct experimental observations of slip lines extending over more than one dislocation cell [58] and in situ crossing through subgrain boundaries [59] confirm the partial transparency of LAGBs.

Possible scenarios to enable the penetration of incident dislocations at the low end of transmission resistances could be: (i) local increase of stress resulting from a pile-up of dislocations ejected from the same source; (ii) activation of dislocation sources in the neighboring subgrain upon reaching their critical stress due to either a similar pile-up or generally increasing plastic incompatibility between both subgrains; (iii) extraction of dislocations from LAGBs resulting from strong fluctuations in the local stress during boundary migration [60]; or (iv) variations in mesh size resulting from the continuous dislocation incidence during (homogeneous) straining, opening up local “holes” in the LAGB.

5. Concluding remarks

We investigated the strengthening ability and dislocation processes associated with a general LAGB simplified as a hexagonal network of dislocations with three Burgers vectors using DDD simulations.

The LAGB poses a major obstacle to dislocation penetration with a wide range of resistances being found to depend on the slip system and line sense of the incident dislocation as well as on the mobility of $\langle 100 \rangle$ dislocation segments in the network. These resistances are directly related to the strength of junctions formed between incident and network dislocations—consistent with the established sequence of increasing strength from binary junctions as the weakest, to ternary junctions, to collinear as the strongest interaction. The latter two reactions might render a boundary impenetrable.

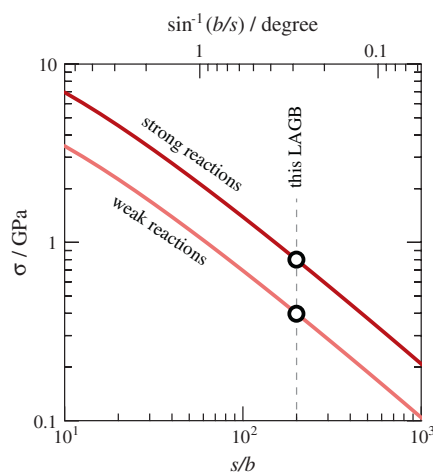


Fig. 8. Estimated dependence of LAGB penetration resistance $\sigma \propto (s/b)^{-1} \ln(s/b)$ on network mesh size s based on penetration strength levels observed at $s/b = 200$ in this study.

³ Defining “steady state” is not without ambiguity (see [57]). Here, approximate constancy of the subgrain size, i.e. LAGB area per volume, is meant.

While the present work strongly simplified the penetration scenario, the situation in a real crystal is far more complex. For example, LAGBs have typically irregular network geometry; are arranged in a (closed) subgrain structure; and experience locally varying stresses promoting or preventing their destabilization. To study more thoroughly the complexity of interactions between a migrating and imperfect LAGB network and the massive flux of individual dislocations traveling through a deforming crystal, much larger numbers of dislocation segments need to be simulated. The necessary amount of memory and computing power is, however, limiting such efforts at present.

Acknowledgements

The authors thank Craig Hartley, Tom Arsenlis, Gregg Hommes, Jaafar El-Awady, Yunzhi Wang, Anter El-Azab, Roger Reed and Adrian Sutton for their support and many helpful discussions. Careful reading of the final manuscript by Ross Marceau is greatly appreciated. The work was in part supported by the Deutsche Forschungsgemeinschaft through contract EI681/2-1.

References

- [1] Kocks U, Argon A, Ashby M. *Prog Mater Sci* 1975;19:1.
- [2] Bay B, Hansen N, Hughes D, Kuhlmann-Wilsdorf D. *Acta Metall Mater* 1992;40(2):205.
- [3] Aernoudt E, Van Houtte P, Leffers T. Plastic deformation and fracture of materials. In: Mughrabi H, Cahn R, Haasen P, Kramer E, editors. *Materials science and technology*, vol. 6. Weinheim: VCH; 1992. p. 89–136.
- [4] Hughes D, Hansen N. *Acta Mater* 1997;45:3871.
- [5] Hughes D, Liu Q, Chrzan D, Hansen N. *Acta Mater* 1997;45(1):105.
- [6] Hughes D. *Scripta Mater* 2002;47:697.
- [7] Raabe D, Sachtleber M, Zhao Z, Roters F, Zaefferer S. *Acta Mater* 2001;49:3433.
- [8] Zhao Z, Ramesh M, Raabe D, Cuitino A, Radovitzky R. *Int J Plast* 2008;24:2278.
- [9] Roters F, Eisenlohr P, Hantcherli L, Tjahjanto DD, Bieler T, Raabe D. *Acta Mater* 2010;58:1152.
- [10] Bulatov V, Abraham F, Kubin L, Devincre B, Yip S. *Nature* 1998;391(6668):669.
- [11] Madec R, Devincre B, Kubin L, Hoc T, Rodney D. *Science* 2003;301(5641):1879.
- [12] Bulatov V, Hsiung L, Tang M, Arsenlis A, Bartelt M, Cai W, et al. *Nature* 2006;440(7088):1174.
- [13] Cheng Y, Mrovec M, Gumbsch P. *Philos Mag* 2008;88:547.
- [14] Cheng Y, Weygand D, Gumbsch P. *Comput Mater Sci* 2009;45:783.
- [15] Bachurin DV, Weygand D, Gumbsch P. *Acta Mater* 2010;58:5232.
- [16] de la Rubia T, Zbib H, Khraishi T, Wirth B, Victoria M, Caturla M. *Nature* 2000;406(6798):871.
- [17] Schwarz K. *Phys Rev Lett* 2003;91(14):145503.
- [18] Fertig R, Baker S. *Prog Mater Sci* 2009;54(6):874.
- [19] Csikor F, Motz C, Weygand D, Zaiser M, Zapperi S. *Science* 2007;318(5848):251.
- [20] Rao S, Dimiduk D, Parthasarathy T, Uchic M, Tang M, Woodward C. *Acta Mater* 2008;56(13):3245.
- [21] Senger J, Weygand D, Gumbsch P, Kraft O. *Scripta Mater* 2008;58(7):587.
- [22] Tang H, Schwarz K, Espinosa H. *Phys Rev Lett* 2008;100(18):185503.
- [23] Schiotz J, Jacobsen K. *Science* 2003;301(5638):1357.
- [24] Van Swygenhoven H, Derlet P, Froseth A. *Nat Mater* 2004;3(6):399.
- [25] Van Swygenhoven H, Derlet P, Froseth A. *Acta Mater* 2006;54(7):1975.
- [26] Zhu T, Li J, Samanta A, Kim H, Suresh S. *Proc Natl Acad Sci* 2007;104(9):3031.
- [27] Li X, Wei Y, Lu L, Lu K, Gao H. *Nature* 2010;464(7290):877.
- [28] Hirth J, Lothe J. *Theory of dislocations*. New York: John Wiley & Sons; 1982.
- [29] Hirth J. *Metall Trans* 1972;3:3047.
- [30] Hull D, Bacon D. *Introduction to dislocations*. Oxford: Butterworth; 2001.
- [31] Queyreau S, Monnet G, Devincre B. *Int J Plast* 2009;25(2):361.
- [32] Arsenlis A, Cai W, Tang M, Rhee M, Oppelstrup T, Hommes G, et al. *Modell Simul Mater Sci Eng* 2007;15(6):553.
- [33] Liu B, Raabe D, Eisenlohr P, Roters F, Arsenlis A, Hommes G. *Acta Mater* 2011;59(19):7125.
- [34] Madec R, Kubin L. *Scripta Mater* 2008;58(9):767.
- [35] Blum W. *Z Metallkd* 1977;68:484.
- [36] Bulatov V, Cai W. *Phys Rev Lett* 2002;89(11):115501.
- [37] Terentyev D, Osetsky Y, Bacon D. *Acta Mater* 2010;58(7):2477.
- [38] Keh A. *Philos Mag* 1965;12(115):9.
- [39] Keh A, Nakada Y. *Can J Phys* 1967;45(2):1101.
- [40] Feltham P. *J Phys D: Appl Phys* 1969;2(3):377.
- [41] Spitzig W, Keh A. *Acta Metall* 1970;18(6):611.
- [42] Franciosi P. *Acta Metall* 1983;31(9):1331.
- [43] Novák V, Šesták B, Zárubová N. *Cryst Res Technol* 1984;19(6):793.
- [44] Basinski S, Basinski Z. *Plastic deformation and work hardening. Dislocations in solids*, vol. 4. Amsterdam: North Holland; 1979. p. 261–362.
- [45] Mughrabi H. *Acta Metall* 1983;31(9):1367.
- [46] Raabe D. *Philos Mag A* 1996;73:1363.
- [47] Straub S, Blum W, Maier H, Borbély A, Ungár T, Renner H. *Acta Mater* 1996;44(11):4337.
- [48] Borbély A, Hoffmann G, Aernoudt E, Ungár T. *Acta Mater* 1997;45(1):89.
- [49] Levine L, Geantil P, Larson B, Tischler J, Kassner M, Liu W, et al. *Acta Mater* 2011;59(14):5803.
- [50] Morris M, Martin J. *Acta Metall* 1984;32(4):549.
- [51] Morris M, Martin J. *Acta Metall* 1984;32(10):1609.
- [52] Blum W. *Nippon Kinzoku Gakkai-ho (Bull Jpn Inst Met)* 1991;30:506.
- [53] Karashima S, Iikubo T, Watanabe T, Oikawa H. *T Jpn Inst Met* 1971;12(5):369.
- [54] Orlová A, Tobolová Z, Čadek J. *Philos Mag* 1972;26(6):1263.
- [55] Kassner M, McMahon M. *Metall Trans A* 1987;18:835.
- [56] Mekala S, Eisenlohr P, Blum W. *Philos Mag* 2011;91(6):908.
- [57] Blum W, Eisenlohr P. *Mater Sci Forum* 2011;683:163.
- [58] Ambrosi P, Schwink C. In: Haasen P, Gerold V, Kosterz G, editors. *Proceedings of the 5th international conference on the strength of metals and alloys (ICSMA 5)*, vol. 1. Oxford: Pergamon Press; 1980. p. 29–33.
- [59] Caillard D. *Acta Metall* 1984;32(9):1483.
- [60] Caillard D, Martin J. *Acta Metall* 1983;31(5):813.